JOURNAL OF COMPUTATIONAL PHYSICS 70, 232–252 (1987)

Time-Marching Solution of Incompressible Navier–Stokes Equations for Internal Flow

W. Y. SOH

Sverdrup Technology Inc., NASA Lewis Research Center, 21000 Brookpark Road, Cleveland, Ohio 44135

Received December 3, 1985; revised August 29, 1986

A factored ADI finite-difference scheme has been developed for solution of the two dimensional incompressible Navier–Stokes equations by the artificial compressibility method. The scheme employs primitive variables with central differencing on a staggered grid. The resulting close coupling between pressure and velocity produces enhanced stability and eliminates the need for artificial damping. A spatially variable time step based on a fixed Courant number is used to improve computational efficiency. Numerical results have been obtained for flows in a straight channel, a curved rotating channel, and a driven cavity. In the latter case at Reynolds number of 10,000 with local cell Reynolds numbers as high as 100, a solution on a 40×40 stretched grid shows no spatial oscillations in the flow variables.

1. INTRODUCTION

The purpose of this study is to obtain solutions of steady, incompressible, internal fluid flow using a time-marching calculation of the Navier–Stokes equations. Unlike the compressible flow case, the continuity equation for incompressible flow has no explicit time derivative terms; the constraint "$\nabla \cdot \mathbf{u} = 0$" must be satisfied at any time t, which makes solving the incompressible momentum equations for either viscous or inviscid flow difficult if a standard time-marching solution method is used.

Taking a curl of the momentum equations gives the vorticity transport equations with the pressure eliminated. This formulation requires the use of the vorticity boundary conditions, which are difficult to implement, especially in three dimensions. Furthermore, the pressure is not obtained directly so that additional calculation is needed. Because of these difficulties, it is advantageous and more straightforward to use the primitive variables, say velocity $\mathbf{u}$ and pressure p, as the dependent variables. The primitive variable formulation is also more accurate on the boundaries.

Harlow and Welch [1] have developed a method of solving the two dimensional unsteady Navier–Stokes equations by employing the Poisson equation for the pressure in such a way that the continuity equation is satisfied at each time step.

0021-9991/87 $3.00

Williams [2] followed a similar procedure in the calculation of a three dimensional natural convection problem with the Fast Fourier Transform technique as a Poisson equation solver for the pressure. Chorin [3] proposed another method which avoids solving the Poisson equation directly by introducing an intermediate step in which the flow velocities are first obtained by solving the momentum equations with the pressure gradients omitted. Then in order to obtain a divergence free velocity field, the velocities are corrected successively by the pressure gradients in the following time step until the continuity equation is satisfied. A variation of the method of reference [3] known as the velocity-pressure method has been widely used [4–6] with many different finite-difference schemes.

If the goal is to obtain the steady solution only, any of these methods are computationally wasteful. Chorin [7] and Temam [8] introduced an effective way to overcome the difficulty inherent in the constraint, "$\nabla \cdot \mathbf{u} = 0$," by adding a time derivative of the pressure to the continuity equation. This term is multiplied by an "artificial compressibility" coefficient. The method has been applied to fluid flow and heat transfer problems in both two and three space dimensions [9–11], and the numerical analysis also has been done extensively [12–14]. An excellent survey of this work has been made by Peyret and Taylor [15].

The present study presents a central-difference numerical scheme coupled with the velocity and pressure without adding artificial damping terms. In Section 2 we discuss a numerical scheme based on the artificial compressibility method along with the boundary conditions and the choice of the artificial compressibility coefficient and the time step. Section 3 provides numerical results on an IBM 370/3033 for channel flows and a driven cavity flow at very large Reynolds number, in which there are no oscillations in the flow variables obtained by the central-difference numerical scheme.

2. Formulation of the Problem

2.1. *Mathematical Formulation*

The Navier–Stokes equations with artificial compressibility can be written in dimensionless form as

$$\frac{\partial \mathbf{u}}{\partial t} + \nabla \cdot (\mathbf{uu}) = -\nabla p + \frac{1}{\mathrm{Re}} \nabla^2 \mathbf{u} \tag{2.1}$$

$$\delta \frac{\partial p}{\partial t} + \nabla \cdot \mathbf{u} = 0 \tag{2.2}$$

where δ and Re are the artificial compressibility coefficient and the Reynolds number, respectively. The divergence free constraint on the velocity has been replaced by a time evolution equation for the pressure, which implies (2.1) and (2.2) can be solved by existing numerical methods for real compressible flow problems. The

major advantage of using the system (2.1) and (2.2) is that no iteration is needed to satisfy "$\nabla \cdot \mathbf{u} = 0$" at each time step. System (2.1) and (2.2) has no physical meaning until steady state is reached.

Introducing the artificial compressibility term, $\delta \partial p/\partial t$, into the continuity equation, in the inviscid limit, results in a system of hyperbolic partial differential equations that gives rise to an artificial wave speed. As an example, let us consider the inviscid one dimensional version of (2.1) and (2.2) as follows:

$$\frac{\partial}{\partial t}\begin{bmatrix} u \\ p \end{bmatrix} + \begin{bmatrix} 2u & 1 \\ 1/\delta & 0 \end{bmatrix} \frac{\partial}{\partial x}\begin{bmatrix} u \\ p \end{bmatrix} = 0. \tag{2.3}$$

The eigenvalues of the square matrix of (2.3) are $u \pm (u^2 + 1/\delta)^{1/2}$, which are real and distinct, therefore (2.3) is hyperbolic. Furthermore, the eigenvalues are opposite in sign; in other words, the flow field described by using artificial compressibility is subsonic for any positive values of δ. This guarantees that there will be no discontinuity, such as a shock in the solution, therefore, δ may be chosen to produce the fastest convergence to the steady state.

2.2. *Numerical Formulation*

In discussing finite-difference formulations of the system (2.1) and (2.2) we will restrict ourselves to a two dimensional analysis in a Cartesian coordinate system, which can be readily extended to three dimensional flows. The factored implicit method of Douglas and Gunn [16] has been employed for compressible flows by Beam and Warming [17] and Briley and McDonald [18]. The present finite-difference scheme uses a similar technique for incompressible flows using a staggered grid system. In this grid system scalar quantities (e.g., pressure in this analysis) are located at the centers of their cells and the velocity components in the x- and y-directions, u and v, are stored at different positions on the boundaries of the pressure cell, as is shown in Fig. 1.

Equations (2.1) and (2.2) can be written as

$$\frac{\partial \boldsymbol{\phi}}{\partial t} + (\mathbf{A}_x + \mathbf{A}_y)\,\boldsymbol{\phi} = 0 \tag{2.4}$$

where

$$\boldsymbol{\phi} = \begin{bmatrix} u \\ v \\ p \end{bmatrix}, \quad \mathbf{A}_x = \begin{bmatrix} M & 0 & \dfrac{\partial}{\partial x} \\ 0 & M & 0 \\ \dfrac{1}{\delta}\dfrac{\partial}{\partial x} & 0 & 0 \end{bmatrix}, \quad \mathbf{A}_y = \begin{bmatrix} N & 0 & 0 \\ 0 & N & \dfrac{\partial}{\partial y} \\ 0 & \dfrac{1}{\delta}\dfrac{\partial}{\partial y} & 0 \end{bmatrix}$$

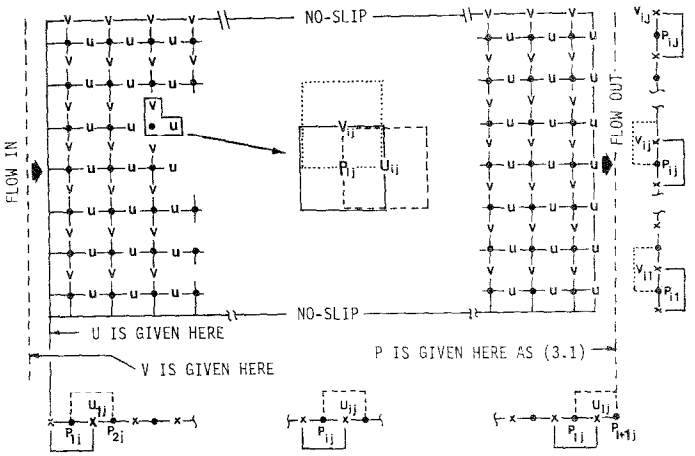

FIG. 1. Staggered grid system and boundary conditions. u, u-velocity; v, v-velocity; ●, pressure; ---, u-; ···, v-; ——, p-cell.

where

$$M\psi = \frac{\partial}{\partial x}(u\psi) - \frac{1}{\mathrm{Re}}\frac{\partial^2\psi}{\partial x^2}, \qquad N\psi = \frac{\partial}{\partial y}(v\psi) - \frac{1}{\mathrm{Re}}\frac{\partial^2\psi}{\partial y^2};$$

here $\psi = u$ or v. Introducing an intermediate step, denoted by *, and approximating the convective terms with the values at the present time $n\,\Delta t$, we can advance (2.4) in time as follows:

$$\begin{aligned} \boldsymbol{\phi}^* - \boldsymbol{\phi}^n + \Delta t(\mathbf{A}_x^n\boldsymbol{\phi}^n + \mathbf{A}_y^n\boldsymbol{\phi}^*) &= 0 \\ \boldsymbol{\phi}^{n+1} - \boldsymbol{\phi}^n + \Delta t(\mathbf{A}_x^n\boldsymbol{\phi}^{n+1} + \mathbf{A}_y^n\boldsymbol{\phi}^*) &= 0. \end{aligned} \tag{2.5}$$

We may consider the first and second expressions of (2.5) as a prediction and a correction step, respectively. The convection terms in N are discretized in the intermediate step, denoted by *, as

$$\frac{\partial}{\partial y}(vu) = \frac{(v_u^+)^n(u_{ij} + u_{ij+1})^*/2 - (v_u^-)^n(u_{ij} + u_{ij-1})^*/2}{\Delta y}$$

$$\frac{\partial}{\partial y}(vv) = \frac{(v_v^+)^n(v_{ij} + v_{ij+1})^*/2 - (v_v^-)^n(v_{ij} + v_{ij-1})^*/2}{\Delta y}$$

where $v_u^+ = (v_{ij} + v_{i+1j})/2$, $v_u^- = (v_{ij-1} + v_{i+1j-1})/2$, $v_v^+ = (v_{ij} + v_{ij+1})/2$, and $v_v^- = (v_{ij} + v_{ij-1})/2$, which represent the v-velocities on the upper and lower boundaries of the u- and v-cells, respectively. For the correction step, denoted by superscript $n+1$, the convective terms in M are discretized as

$$\frac{\partial}{\partial x}(uv) = \frac{(u_v^+)^n(v_{ij}+v_{i+1j})^{n+1}/2 - (u_v^-)^n(v_{ij}+v_{i-1j})^{n+1}/2}{\Delta x}$$

$$\frac{\partial}{\partial x}(uu) = \frac{(u_v^+)^n(u_{ij}+u_{i+1j})^{n+1}/2 - (u_u^-)^n(u_{ij}+u_{i-1j})^{n+1}/2}{\Delta x}$$

where $u_v^+ = (u_{ij}+u_{ij+1})/2$, $u_v^- = (u_{i-1j}+u_{i-1j+1})/2$, $u_u^+ = (u_{ij}+u_{i+1j})/2$, and $u_u^- = (u_{ij}+u_{i-1j})/2$, which are the u-velocities on the right and left side boundaries of the v- and u-cells, respectively.

Obviously, the converged solution of (2.5) is a steady-state solution of (2.4). System (2.5) can be rewritten in a simpler "delta form" as

$$(\mathbf{I} + \Delta t\, \mathbf{A}_y^n)\, \Delta\boldsymbol{\phi}^* = -\Delta t(\mathbf{A}_x^n + \mathbf{A}_y^n)\, \boldsymbol{\phi}^n \tag{2.6}$$

$$(\mathbf{I} + \Delta t\, \mathbf{A}_x^n)\, \Delta\boldsymbol{\phi}^{n+1} = \Delta\boldsymbol{\phi}^* \tag{2.7}$$

where $\Delta\boldsymbol{\phi}^* = \boldsymbol{\phi}^* - \boldsymbol{\phi}^n$, $\Delta\boldsymbol{\phi}^{n+1} = \boldsymbol{\phi}^{n+1} - \boldsymbol{\phi}^n$, and $\mathbf{I}$ is the identity matrix. Finally, (2.6) and (2.7) can be combined to yield

$$(\mathbf{I} + \Delta t(\mathbf{A}_y^n + \mathbf{A}_x^n) + \Delta t^2\, \mathbf{A}_y^n \mathbf{A}_x^n)\, \Delta\boldsymbol{\phi}^{n+1} = -\Delta t(\mathbf{A}_y^n + \mathbf{A}_x^n)\, \boldsymbol{\phi}^n. \tag{2.8}$$

Let us call the calculation procedure of (2.6) the y-sweep, and (2.7) the x-sweep, and express them in central spatial difference form. Then in the staggered grid system:

For the y-sweep:

$$\left(-\frac{t_y}{2}v_u^- - t_y'\right)\Delta u_{ij-1}^* + \left(1 + \frac{t_y}{2}(v_u^+ - v_u) + 2t_y'\right)\Delta u_{ij}^* + \left(\frac{t_y}{2}v_u^+ - t_y'\right)\Delta u_{ij+1}^* = (Ru)_{ij} \tag{2.9}$$

$$\begin{bmatrix} -\frac{t_y}{2}v_v^- - t_y' & 0 \\ -\frac{t_y}{\delta} & 0 \end{bmatrix} \begin{bmatrix} \Delta v \\ \Delta p \end{bmatrix}_{ij-1}^* + \begin{bmatrix} 1 + \frac{t_y}{2}(v_v^+ - v_v^-) + 2t_y' & -t_y \\ \frac{t_y}{\delta} & 1 \end{bmatrix} \begin{bmatrix} \Delta v \\ \Delta p \end{bmatrix}_{ij}^* + \begin{bmatrix} \frac{t_y}{2}v_v^+ - t_y' & t_y \\ 0 & 0 \end{bmatrix} \begin{bmatrix} \Delta v \\ \Delta p \end{bmatrix}_{ij+1}^* = \begin{bmatrix} Rv \\ Rp \end{bmatrix}_{ij}, \quad \begin{matrix} i = 1, 2, \ldots, I \\ j = 1, 2, \ldots, J \end{matrix} \tag{2.10}$$

where $t_y = \Delta t/\Delta y$, $t_y' = \Delta t/(\mathrm{Re}\,\Delta y^2)$. $(Ru)_{ij}$ and $(Rv)_{ij}$ are the central-difference expressions of the x, y components of $\Delta t(\mathrm{Re}^{-1}\nabla^2\mathbf{u} - \nabla p - \nabla\cdot(\mathbf{uu}))^n$ at the u- and v-cells, respectively, and $(Rp)_{ij}$ is the two-point central-difference formulation of $-\Delta t(\nabla\cdot\mathbf{u})^n/\delta$ at the p-cell. As shown above, in the y-sweep Δu^* is decoupled from the pressure and treated as a scalar, whereas Δv^* and Δp^* are coupled to yield a

2×2 block tridiagonal matrix. Also, note from (2.10) that $\partial p/\partial y$ for the v-momentum and $\partial v/\partial y$ for the continuity equation are approximated by two-point central-difference relations.

For the x-sweep:

$$\left(-\frac{t_x}{2}u_v^- - t'_x\right)\Delta v_{i-1j}^{n+1} + \left(1+\frac{t_x}{2}(u_v^+ - u_v^-) + 2t'_x\right)\Delta v_{ij}^{n+1} + \left(\frac{t_x}{2}u_v^+ - t'_x\right)\Delta v_{i+1j}^{n+1} = \Delta v_{ij}^* \tag{2.11}$$

$$\begin{bmatrix} -\frac{t_x}{2}u_u^- - t'_x & 0 \\ -\frac{t_x}{\delta} & 0 \end{bmatrix}\begin{bmatrix}\Delta u \\ \Delta p\end{bmatrix}_{i-1j}^{n+1} + \begin{bmatrix} 1+\frac{t_x}{2}(u_u^+ - u_u^-) + 2t'_x & -t_x \\ \frac{t_x}{\delta} & 1 \end{bmatrix}\begin{bmatrix}\Delta u \\ \Delta p\end{bmatrix}_{ij}^{n+1}$$
$$+ \begin{bmatrix} \frac{t_x}{2}u_u^+ - t'_x & t_x \\ 0 & 0 \end{bmatrix}\begin{bmatrix}\Delta u \\ \Delta p\end{bmatrix}_{i+1j}^{n+1} = \begin{bmatrix}\Delta u \\ \Delta p\end{bmatrix}_{ij}^{*} \tag{2.12}$$

where $t_x = \Delta t/\Delta x$, $t'_x = \Delta t/(\mathrm{Re}\,\Delta x^2)$. In the x-sweep, Δv^{n+1} becomes decoupled from the pressure while Δu^{n+1} and Δp^{n+1} form a 2×2 block matrix. Also $\partial p/\partial x$ in the u-momentum and $\partial u/\partial x$ in the continuity equation again have two-point central-difference approximations.

The velocity and pressure coupling in the x- and y-sweeps is illustrated in Fig. 1. The details in the finite-difference expressions of $(Ru)_{ij}$, $(Rv)_{ij}$, $(Rp)_{ij}$ and others are shown in the Appendix.

2.3. *Boundary Conditions*

In the staggered grid arrangements the pressure boundary condition is not required on the physical boundary, which is a solid wall in this work. In internal flow problems, such as a channel flow, no-slip conditions are imposed on the solid boundaries. For the inlet and exit let us examine the behavior of the characteristics of the inviscid equations of motion as

$$\frac{\partial}{\partial t}\begin{bmatrix}u\\v\\p\end{bmatrix} + \begin{bmatrix}2u & 0 & 1\\ v & u & 0\\ 1/\delta & 0 & 0\end{bmatrix}\frac{\partial}{\partial x}\begin{bmatrix}u\\v\\p\end{bmatrix} + \begin{bmatrix}v & u & 0\\ 0 & 2v & 1\\ 0 & 1/\delta & 0\end{bmatrix}\frac{\partial}{\partial y}\begin{bmatrix}u\\v\\p\end{bmatrix} = 0. \tag{2.13}$$

Since the characteristics of the first square matrix are u, $u\pm(u^2+1/\delta)^{1/2}$, two right running waves at the inlet and one left running wave at the exit propagate into the computational domain. Therefore, two boundary conditions are imposed at the inlet, and only one at the exit. In this work we specify the velocities, u and v, at the inlet and the pressure at the exit, as shown in Fig. 1.

2.4. *Choice of Artificial Compressibility and Time Step*

To have some idea how to choose the artificial compressibility coefficient, δ, we take the linear combination of the first and second square matrices of (2.13), which are denoted by $\mathbf{C}_x$ and $\mathbf{C}_y$, as

$$\mathbf{D} = \alpha_1 \mathbf{C}_x + \alpha_2 \mathbf{C}_y \tag{2.14}$$

where α_1 and α_2 are numbers chosen to be $\cos\theta$ and $\sin\theta$; here θ is any value of angle. The matrix $\mathbf{D}$ can be diagonalized to yield the eigenvalues, λ's as

$$\lambda = c, \qquad c \pm [c^2 + (\alpha_1^2 + \alpha_2^2)/\delta]^{1/2}, \qquad \alpha_1^2 + \alpha_2^2 = 1 \tag{2.15}$$

where $c = \alpha_1 u + \alpha_2 v$. If a local impulsive plane perturbation front is introduced to the solution of (2.13), plane waves propagate with velocities of λ's in a direction perpendicular to the perturbation front; then θ is the angle between the x-axis and this direction (see p. 6, Ref. [19]). We choose δ in such a way that the magnitudes of the eigenvalues are of the same order as

$$c \sim c + (c^2 + 1/\delta)^{1/2} \qquad \text{and} \qquad c \sim |c - (c^2 + 1/\delta)^{1/2}|.$$

From the second expression above we have $\delta \sim 1/3c^2$. In this case the ratio of the largest eigenvalue to the smallest one is only about 3. In the present work we take δ as

$$\delta = \frac{1}{3q^2} \tag{2.16}$$

where q, which is $u^2 + v^2$, is some representative flow speed. For the optimum value of δ a physical understanding or qualitative estimation of the flow field under consideration and numerical experiments are needed.

For the choice of an appropriate time step, Δt, let us consider the linearized inviscid equations in a non-conservative form as

$$\frac{\partial \mathbf{u}}{\partial t} + (\mathbf{u}_0 \cdot \nabla)\,\mathbf{u} = -\nabla p, \qquad \delta \frac{\partial p}{\partial t} + \nabla \cdot \mathbf{u} = 0 \tag{2.17}$$

where $\mathbf{u}_0$ is the local velocity with (u_0, v_0) in the x and y directions, respectively, and it is assumed constant. After discretizing (2.17) in the central-difference form for the staggered grid we replace (u, v, p) by their Fourier components $(U, V, P)\exp(i\mathbf{k}\cdot\mathbf{x})$, where $i = \sqrt{-1}$, $\mathbf{k}$ is the wave number with components (k_x, k_y) and $\mathbf{x}$ is the position vector. Then we have from the present scheme described in (2.8)

$$\begin{bmatrix} U \\ V \\ P \end{bmatrix}^{n+1} = \mathbf{G} \begin{bmatrix} U \\ V \\ P \end{bmatrix}^{n}, \qquad \mathbf{G} = (\mathbf{I} + \Delta t(\hat{\mathbf{A}}_y + \hat{\mathbf{A}}_x) + \Delta t^2\, \hat{\mathbf{A}}_y \hat{\mathbf{A}}_x)^{-1}(\mathbf{I} + \Delta t^2 \hat{\mathbf{A}}_y \hat{\mathbf{A}}_x) \tag{2.18}$$

where

$$\hat{\mathbf{A}}_y = \begin{bmatrix} \dfrac{iv_0 \sin\beta}{\Delta y} & 0 & 0 \\ 0 & \dfrac{iv_0 \sin\beta}{\Delta y} & \dfrac{e^{i\beta}-1}{\Delta y} \\ 0 & \dfrac{1-e^{-i\beta}}{\delta\,\Delta y} & 0 \end{bmatrix}, \qquad \hat{\mathbf{A}}_x = \begin{bmatrix} \dfrac{iu_0 \sin\alpha}{\Delta x} & 0 & \dfrac{e^{i\alpha}-1}{\Delta x} \\ 0 & \dfrac{iu_0 \sin\alpha}{\Delta x} & 0 \\ \dfrac{1-e^{-i\alpha}}{\delta\,\Delta x} & 0 & 0 \end{bmatrix}$$

and $\alpha = k_x \Delta x$, $\beta = k_y \Delta y$. For the purpose of estimating the time step we assume that the Δt^2 term in (2.18) is much smaller than the Δt term so that the amplification matrix can be approximated as

$$\mathbf{G} = [\mathbf{I} + \Delta t(\hat{\mathbf{A}}_y + \hat{\mathbf{A}}_x)]^{-1}.$$

Then, the eigenvalues of $\mathbf{G}$ for the inviscid equations become

$$\lambda(\mathbf{G}) = \frac{1}{1+iQ\,\Delta t}, \qquad \frac{1}{1+i\,\Delta t\left\{\dfrac{Q}{2} \pm \left[\dfrac{Q^2}{4} + \dfrac{2}{\delta}\left(\dfrac{1-\cos\alpha}{\Delta x^2} + \dfrac{1-\cos\beta}{\Delta y^2}\right)\right]^{1/2}\right\}}$$

where $Q = u_0 \sin\alpha/\Delta x + v_0 \sin\beta/\Delta y$. For a minimum $|\lambda|$, it may be a proper choice if we take the following value of the Courant number, Cr, defined as

$$\mathrm{Cr} = \Delta t\left\{C_0 + \left[C_0^2 + \frac{2}{\delta}\left(\frac{1}{\Delta x^2} + \frac{1}{\Delta y^2}\right)\right]^{1/2}\right\}, \qquad \text{where} \quad C_0 = \frac{1}{2}\left(\frac{|u_0|}{\Delta x} + \frac{|v_0|}{\Delta y}\right) \tag{2.19}$$

to be as large as possible. This suggests that a spatially variable time step be used for a fixed Cr.

3. Examples of Calculations

As example problems, fluid flow through a straight channel, a rotating passage, and a driven-cavity flow are presented. Two examples of the through-flow have many practical applications. Computationally, they are good examples of the application of in- and out-flow boundary conditions. The flow in the rotating passage example is of interest in the present two-dimensional study since the flow variables are the functions of two independent space variables even though there are three velocity components. Finally, the driven-cavity flow example is typical of a problem with no preferred flow direction. Furthermore, this example is a model problem of a recirculating flow in a confined region. The boundary condition for this problem is well defined, and is the only specified velocity on the wall.

3.1. *Fluid Flow in a Straight Channel*

Because of the symmetry of the flow, calculations have been performed in half of the flow domain, between the lower wall, $y = 0$, and the center line, $y = H/2$, where H is the channel width. The Reynolds number is defined as $\mathrm{Re} = UH/\nu$, where U is the uniform inlet velocity and ν the kinematic viscosity. At the inlet u and v are set to unity and zero, respectively, and the pressure is allowed to vary. On the wall $u = v = 0$, and along the center line $\partial u/\partial y = v = 0$. At the exit u and v are linearly

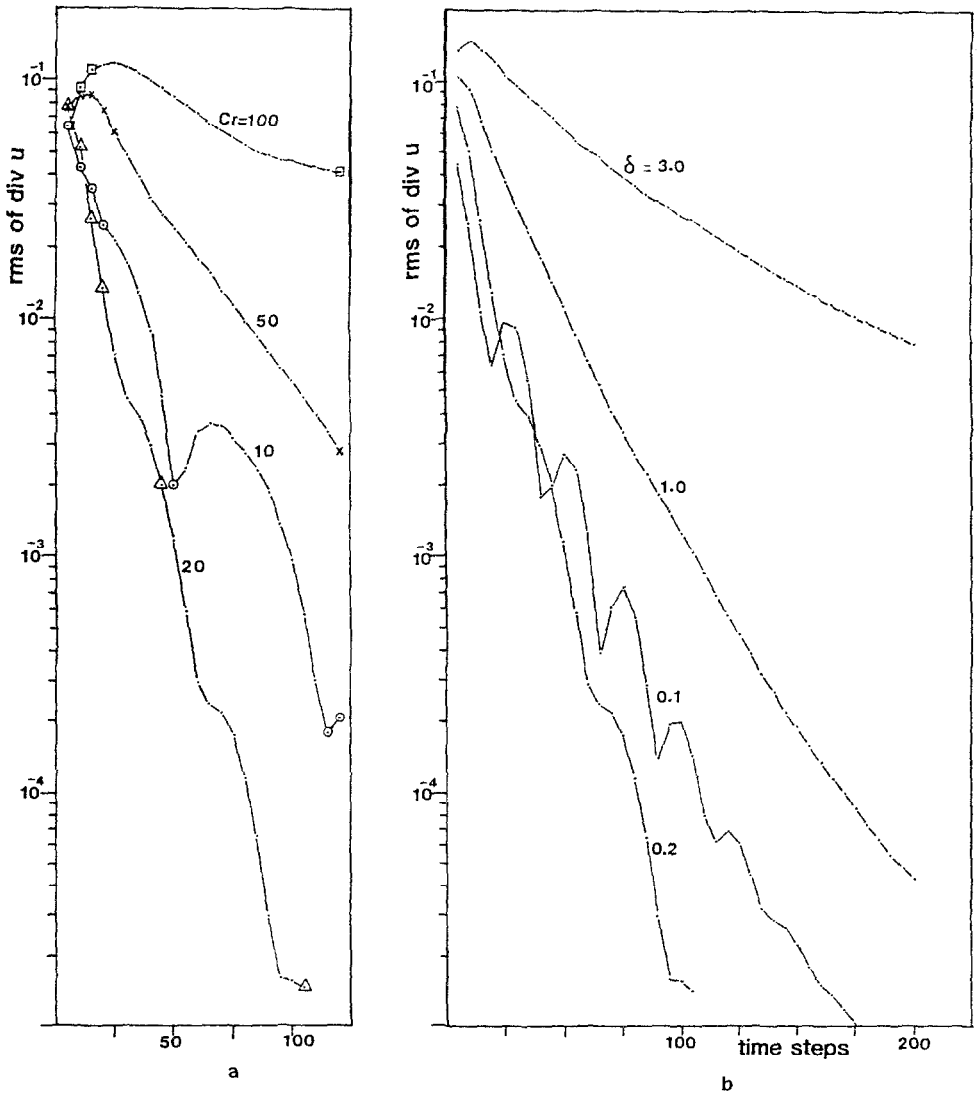

FIG. 2. Convergence rate of rms of $\nabla \cdot \mathbf{u}$ for $\mathrm{Re} = 150$ with a 60×10 grid. (a) Against Cr at $\delta = 0.4$. (b) Against δ at $\mathrm{Cr} = 20$.

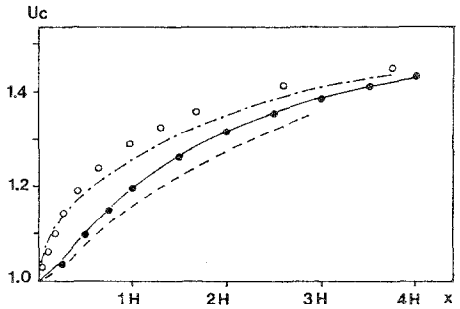

FIG. 3. The u-velocity along a center line of the channel at Re = 150. ○, numerical solution [23]; ●, numerical solution interpolated from Re = 50, 100, and 200 [20]; – · –, 1-term downstream expansion [22]; ——, 2-term upstream expansion [21]; ——, present result.

extrapolated in order to calculate their momentum equations at the very end cells in the x-direction and p is given for the calculation of the u-momentum equation as

$$(p-p_w)_e=\int_0^y\left(\mathrm{Re}^{-1}\frac{\partial^2 v}{\partial y^2}-\frac{\partial}{\partial x}(uv)\right)_e dy-\left(\frac{\partial v}{\partial y}+v^2\right)_e \tag{3.1}$$

where subscripts w and e denote the wall and exit, respectively. It is necessary to fix the pressure level, therefore, $(p_w)_e$ is set to zero.

Figure 2a shows the convergence histories of the rms (root-mean-square) of $\nabla\cdot\mathbf{u}$ for various values of Cr. It is noted that fast convergence is obtained at about Cr = 20 for a fixed δ, 0.4 in this case. A uniform grid with $\Delta y/\Delta x = 0.5$ and Cr = 20 have been used throughout the computations of this example. The rate of convergence is plotted in Fig. 2b for different values of δ at Cr = 20. Taking a representative flow speed to be 1.5 (fully developed maximum velocity) and 0.75 (half of the maximum speed), by (2.16) we may guess the optimum range of δ to be $0.148 \sim 0.592$. Fast convergence is obtained when δ is taken to be about 0.4; slower convergences are observed if δ deviates from 0.4.

It is assumed that the steady state is reached if the maximum value of divergence of the velocity, $\max(\nabla\cdot\mathbf{u})$, is less than 5×10^{-5}. To obtain the steady solution for Re = 150, 105 time steps (18 seconds of CPU time) are needed using a 60×10 grid. The difference in the flow rates between the inlet and outlet is 0.006% of the inlet flow rate and the rms of $\nabla\cdot\mathbf{u}$ converges down to 1.4×10^{-5}. As shown in Fig. 3, the

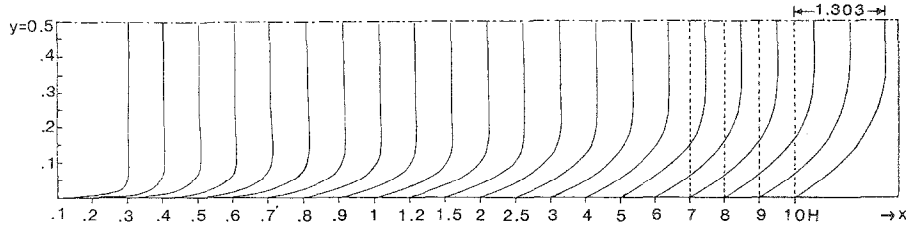

FIG. 4. Development of u-velocity along x for Re = 1000.

present values of u along the center line agree very well with those of Gillis and Brandt [20] for the entire flow region and also with those of Van Dyke [21] in the very inlet region. Figure 4 shows the flow development for $\mathrm{Re} = 1000$. The 100×10 grid, which extends the computational domain up to 10H in the x-direction, was used taking $\delta = 0.4$. The convergence criterion is the same as the case with $\mathrm{Re} = 150$; 175 time steps, which requires 50 seconds CPU time, are needed for the steady state, yielding an rms of $\nabla \cdot \mathbf{u}$ of 5.6×10^{-6} and an error in the flow rates between the inlet and stream of 0.002%. As we can see in Fig. 4 a downstream distance of 10H is not sufficient for a fully developed flow, and there still exists a potential core with a maximum velocity $u = 1.303$.

3.2. *Flow in a Rotating Passage*

Flow in a rotating passage is considered for the geometry shown in the inset of Fig. 5, in which a curved passage without blades is under rotation about the X-axis with an angular velocity $\boldsymbol{\omega}'$. Let us define a reduced pressure, p'', as

$$p'' = p' - \frac{\rho}{2}(\boldsymbol{\omega}' \times \mathbf{r}') \cdot (\boldsymbol{\omega}' \times \mathbf{r}')$$

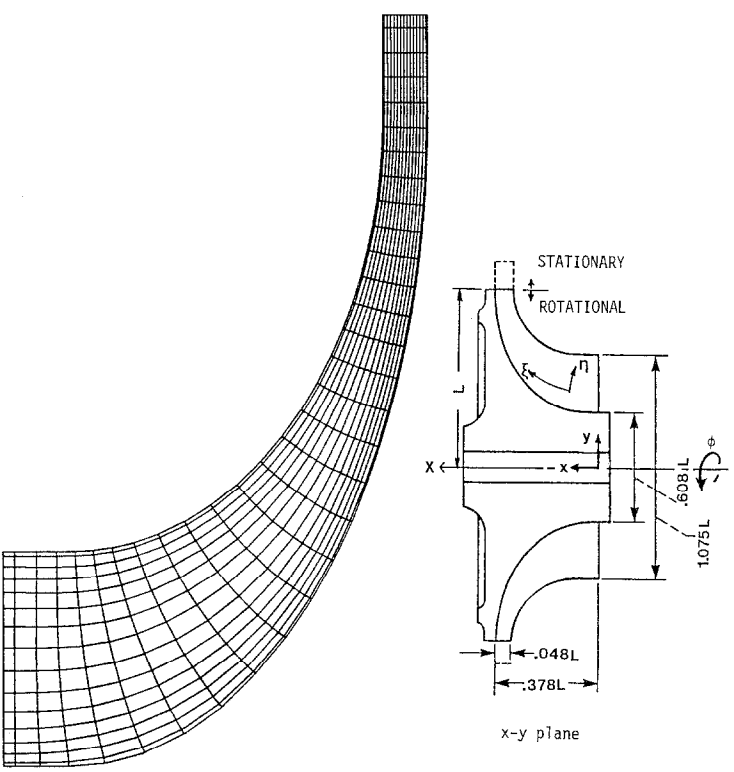

FIG. 5. Orthogonal curvilinear coordinate system.

where $\mathbf{r}'$ is the displacement from the X-axis, p' the static pressure, and ρ the density. If we non-dimensionalize $\mathbf{r}'$, $\mathbf{u}'$, t, and p'' with, respectively, the reference length L (distance from the X-axis to the tip of the rotating part of the wheel in this study), the uniform inlet velocity U, L/U, and ρU^2, we have the Navier–Stokes equations in the rotating frame as (2.1) and (2.2) with the Coriolis force term, $2\varepsilon\mathbf{i}\times\mathbf{u}$, in the left-hand side of the momentum equation. Here Re is the Reynolds number again defined as UL/ν, $\varepsilon = |\boldsymbol{\omega}'|\, L/U$, $\mathbf{u}$ the relative velocity about the X-axis, and $\mathbf{i}$ the unit vector in the X-direction.

The cross-sectional flow area cut by a plane comprising the X-axis, which is called the x–y plane, is transformed into a computational domain (ξ, η) using the numerical orthogonal mapping [24], which is shown in Fig. 5. The artificially compressible Navier–Stokes equations in a weak conservative form are written for the orthogonal coordinate system as

$$
\begin{aligned}
&\frac{\partial u_l}{\partial t} + \frac{1}{\sqrt{g}}\frac{\partial}{\partial x_m}\left(\frac{\sqrt{g}}{h_m}u_l u_m\right) + \frac{u_m}{h_l h_m}\left(u_l\frac{\partial h_l}{\partial x_m} - u_m\frac{\partial h_m}{\partial x_l}\right) + C_l \\
&\quad = -\frac{1}{h_l}\frac{\partial p}{\partial x_l} + \mathrm{Re}^{-1}\left\{\nabla^2 u_l + \frac{1}{\sqrt{g}}\left[\frac{\partial}{\partial x_l}\left(\frac{\sqrt{g}}{h_l^3 h_m}\frac{\partial h_l}{\partial x_m}u_m\right) - \frac{\partial}{\partial x_m}\left(\frac{\sqrt{g}}{h_l^2 h_m^2}\frac{\partial h_m}{\partial x_l}u_m\right)\right]\right. \\
&\qquad + \frac{1}{h_l^2 h_m}\frac{\partial h_l}{\partial x_m}\frac{\partial u_m}{\partial x_l} - \frac{1}{h_l h_m^2}\frac{\partial h_m}{\partial x_l}\frac{\partial u_m}{\partial x_m} - \frac{1}{h_l^2 h_m^2}\left(\frac{\partial h_l}{\partial x_m}\right)^2 u_l \\
&\qquad + \left(\frac{1}{h_l h_m^3}\frac{\partial h_m}{\partial x_m}\frac{\partial h_m}{\partial x_l} + \frac{2}{h_l^3 h_m}\frac{\partial h_l}{\partial x_l}\frac{\partial h_l}{\partial x_m} - \frac{1}{h_l^2 h_m^2}\frac{\partial h_l}{\partial x_m}\frac{\partial h_m}{\partial x_l}\right)u_m \\
&\qquad \left. - \frac{u_n}{h_l h_m^2 h_n}\frac{\partial h_m}{\partial x_l}\frac{\partial h_m}{\partial x_n}\right\} \\
&\delta\frac{\partial p}{\partial t} + \frac{1}{\sqrt{g}}\frac{\partial}{\partial x_m}\left(\frac{\sqrt{g}}{h_m}u_m\right) = 0 \qquad \text{(subscripts } l, m, n \text{ vary from 1 to 3, no sum on } l\text{)}
\end{aligned}
\tag{3.2}
$$

Here (x_1, x_2, x_3) and (u_1, u_2, u_3) correspond to (ξ, η, ϕ) and (u, v, w), respectively, where ϕ is the circumferential angle, and w is the relative velocity in that direction, $h_1 = [(\partial x/\partial\xi)^2 + (\partial y/\partial\xi)^2]^{1/2}$, $h_2 = [(\partial x/\partial\eta)^2 + (\partial y/\partial\eta)^2]^{1/2}$, $h_3 = y$, $\sqrt{g} = h_1 h_2 h_3$, ∇^2 is the Laplacian operator, and C_l is the lth component of the Coriolis force (i.e., $2\varepsilon\mathbf{i}\times\mathbf{u}$).

We take ε, δ, and Re to be 1, 0.3, and 1000, respectively. For the flow independent of ϕ (i.e., $\partial/\partial\phi = 0$) there is no pressure term in the w-momentum equation described in (3.2). Therefore, two different Courant numbers are used for the calculations of the u-, v-, p-equations, and w-equation (which is decoupled from the modified continuity equation) setting $\Delta\xi = \Delta\eta = 1$ by

$$\mathrm{Cr} = \Delta t \left\{ \frac{1}{2}\left(\frac{|u|}{h_1} + \frac{|v|}{h_2}\right) + \left[\frac{1}{4}\left(\frac{|u|}{h_1} + \frac{|v|}{h_2}\right)^2 + \frac{2}{\delta}\left(\frac{1}{h_1^2} + \frac{1}{h_2^2}\right)\right]^{1/2} \right\},$$
$$\mathrm{Crw} = \Delta t \left(\frac{|u|}{h_1} + \frac{|v|}{h_2}\right). \tag{3.3}$$

A uniform velocity (i.e., $u = 1$) is given at the inlet, and the pressure at the exit is given in the same manner as in (3.1). A 28×14 grid is used with $\mathrm{Cr} = 10$ and $\mathrm{Crw} = 5$. At time step 330, $\max(\nabla \cdot \mathbf{u})$ becomes 1.0×10^{-4} with negligible error in the flow rates between the inlet and exit. Comparison of the results between the absolute frame calculation and the relative frame shows an insignificant difference in the flow variables.

Figure 6 shows the development of the main and circumferential flows along the curved passage. It is noted that in the near entrance region the u-profile has the form of a potential vortex in such a way that u increases as η varies from the concave to convex surfaces.

3.3. *Driven Cavity Flow*

As a last example, fluid flow in a driven square cavity is considered for $\mathrm{Re} = 400$ to 10000. The Re is based on the constant velocity with which the upper wall, $y = 1$, is moving in the x-direction. Unlike a through-flow case, it is not easy to pick up a

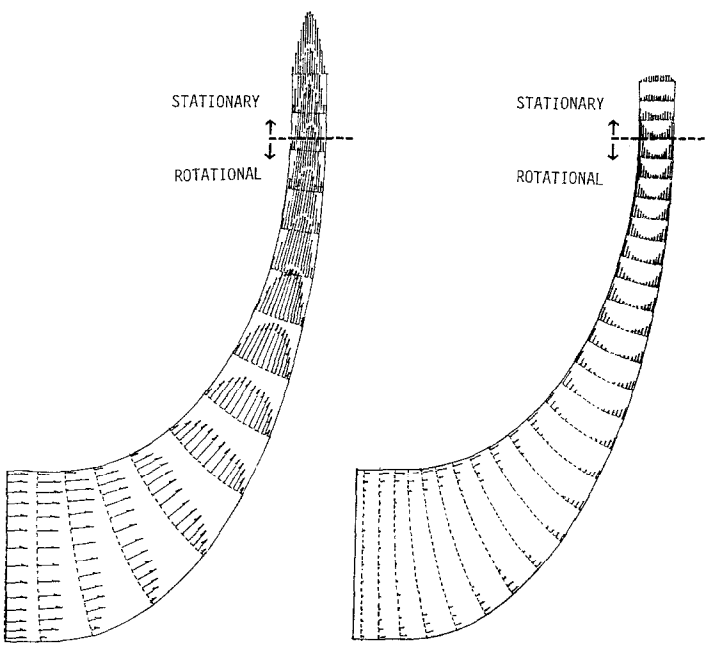

FIG.6. *Left*: Main flow velocity distributions along the channel. *Right*: Absolute circumferential velocity distribution.

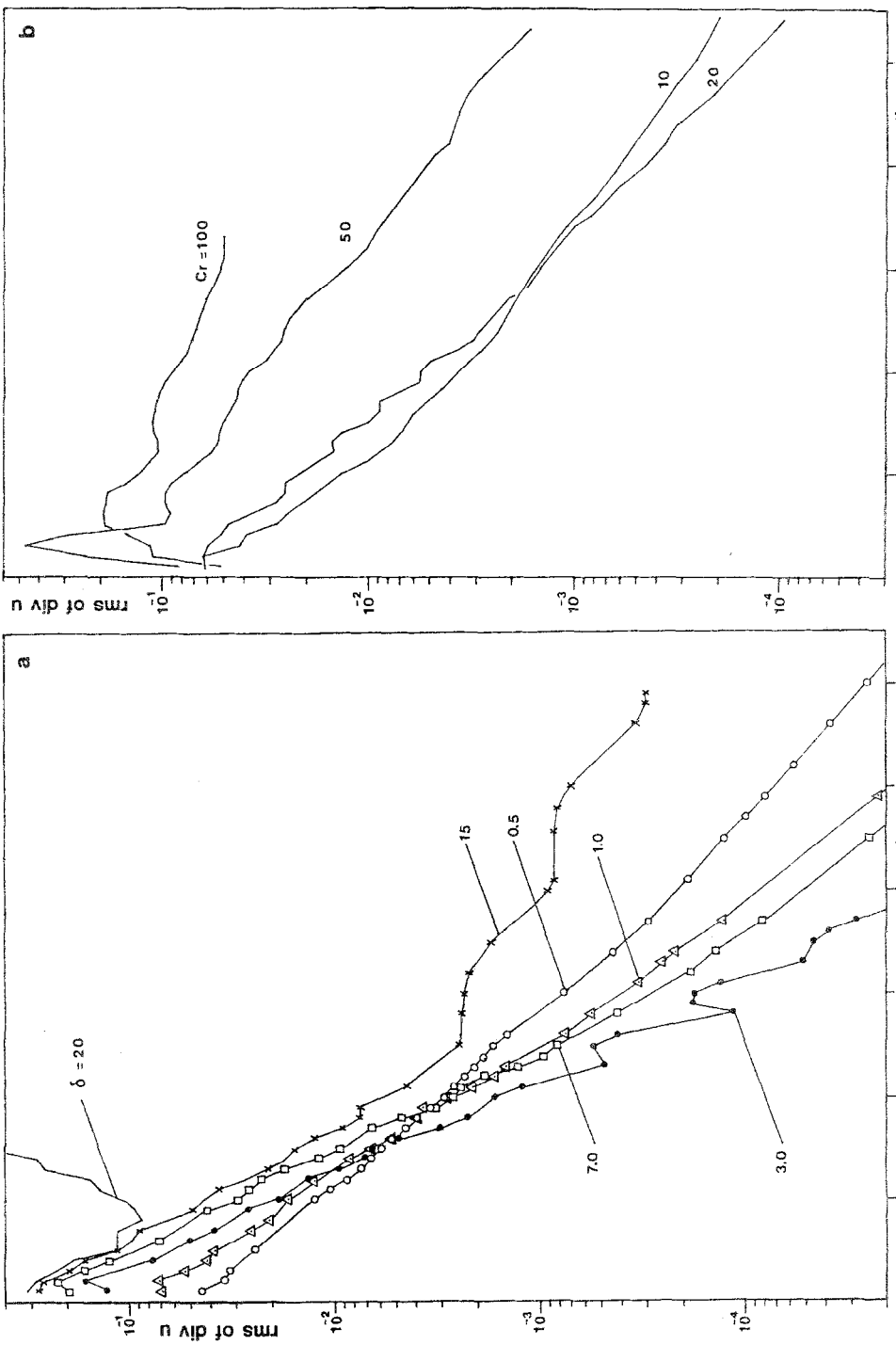

FIG. 7. The convergence rate of rms of $\nabla \cdot \mathbf{u}$. (a) $\mathrm{Re} = 400$ at $\mathrm{Cr} = 20$ in a 20×20 uniform grid; (b) $\mathrm{Re} = 1000$ at $\delta = 1.3$ in a 40×40 uniform grid.

representative speed, q, for the estimation of δ using (2.16). For a flow with no preferred flow direction, like a recirculating flow, q depends highly on the Re and grid used.

Figure 7a demonstrates the convergence rates against various δ for $\mathrm{Cr} = 20$ at $\mathrm{Re} = 400$ using a 20×20 uniform grid. It can be observed that an optimum value of δ is about 3, which corresponds to $q = 0.33$. A severe deviation from it results in slow convergence, and eventually the solution diverges for large δ, 20 in this illustration. In Figure 7b the convergence histories are plotted against Cr for $\mathrm{Re} = 1000$ with the 40×40 uniform grid for a fixed δ of 1.3. For very large Cr, 100, for example, the present scheme yields very slow convergence or may not even converge to a satisfactory level. This indicates that the $\Delta t^2 \mathbf{A}_y \mathbf{A}_x$ term in (2.8), which makes our system (2.8) inconsistent with the Navier–Stokes equations (2.4), has an adverse effect on our scheme for large Cr. Taking the Cr as about 20 is a good choice in this case.

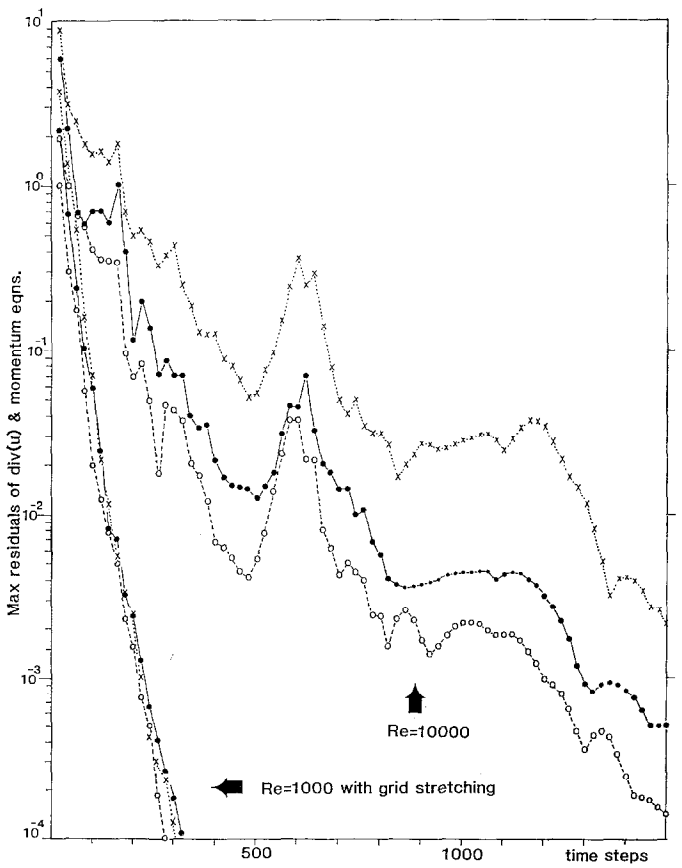

FIG. 8. The convergence rate of the max $(\nabla \cdot \mathbf{u})$ and maximum residuals of momentum equations. ●, $\max(\nabla \cdot \mathbf{u})$; ○, x, the maximum residuals of the u- and v-momentum equations, respectively.

The $\max(\nabla \cdot \mathbf{u})$, maximum residuals of the u- and v-momentum equations are shown in Fig. 8 for $\mathrm{Re} = 1000$ and 10,000. Each quantity for $\mathrm{Re} = 1000$ drops rapidly with almost the same rate. For $\mathrm{Re} = 10{,}000$ the convergence is slow and oscillatory as well. It is noted that the maximum residual of the v-momentum equation is much larger than the other quantities.

The u-velocity profiles with y at the geometric center of the cavity (i.e., $x = 0.5$) are presented in Fig. 9. The results for $\mathrm{Re} = 400$ and 1000, which are obtained using the 40×40 uniform grid, are shown in Fig. 9a and b. The agreement with Ghia *et al.* [25] is excellent, especially for $\mathrm{Re} = 400$, but it is noticeable in Fig. 9b that for a higher Re, say 1000, the present result deviates from theirs (see the maximum value of u near $y = 0$). This is probably due to the fact that at high Re viscous effects are concentrated very close to the walls; therefore, finer grid resolution is needed as Re increases. Although a dense uniform grid could be applied to the entire flow domain, it would increase computation time. An alternative way is to arrange a finer grid near the walls while keeping the total number of grid points unchanged by stretching the coordinates using the transformation functions as

$$x = \frac{\mathrm{Tan}^{-1}[\gamma(2\xi/II - 1)] + \mathrm{Tan}^{-1}\gamma}{2\,\mathrm{Tan}^{-1}\gamma}, \qquad y = \frac{\mathrm{Tan}^{-1}[\gamma(2\eta/JJ - 1)] + \mathrm{Tan}^{-1}\gamma}{2\,\mathrm{Tan}^{-1}\gamma} \tag{3.4}$$

where II and JJ are the numbers of grid points in the x and y directions, and γ is a factor to control the grid. The Navier–Stokes equations in the (ξ, η) coordinate system are written in a conservative form in such a way that all of the metric components are kept inside the derivatives.

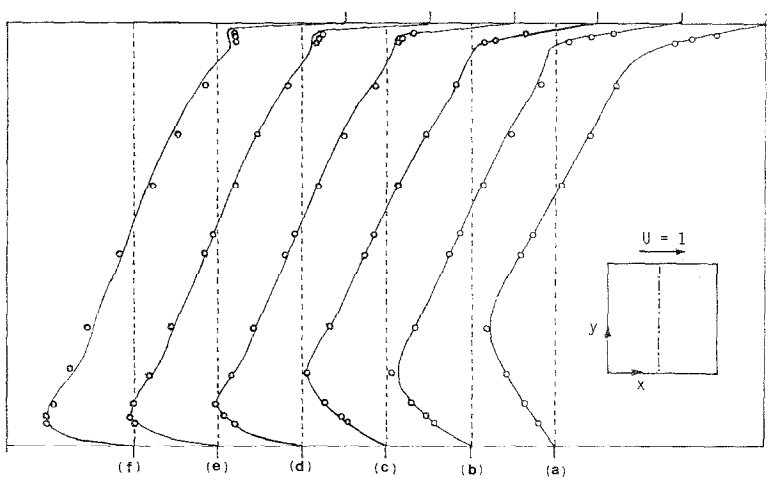

FIG. 9. The u-velocity profiles with y at the center of the cavity (i.e., at $x = 0.5$) using a 40×40 grid. (a) $\mathrm{Re} = 400$, uniform grid. (b) $\mathrm{Re} = 1000$, uniform grid. (c) $\mathrm{Re} = 1000$, non-uniform grid. (d) $\mathrm{Re} = 3200$, non-uniform grid. (e) $\mathrm{Re} = 5000$, non-uniform grid. (f) $\mathrm{Re} = 10000$, non-uniform grid; ○, results obtained by a 129×129 grid [25].

TABLE I

Run Conditions and Results for the Driven-Cavity Flow Using a 40×40 Grid

	Re	Cr	δ	γ	Time steps	max($\nabla \cdot \mathbf{u}$)	rms($\nabla \cdot \mathbf{u}$)	CPU time (in sec)	y_{max}	u_{max}
a	400	20	10	—	350	1.0×10^{-4}	7.06×10^{-6}	156	0.288	−0.312
b	1000	20	3	—	300	1.0×10^{-4}	2.59×10^{-5}	137	0.181	−0.348
c	1000	20	3	1.5	320	1.0×10^{-4}	1.49×10^{-5}	162	0.185	−0.372
d	3200	10	2	2.5	600	6.2×10^{-4}	1.45×10^{-4}	305	0.095	−0.407
e	5000	10	3	3.0	800	7.2×10^{-4}	1.78×10^{-4}	396	0.081	−0.415
f	10000	10	5	4.0	1500	5.0×10^{-4}	1.10×10^{-4}	729	0.075	−0.409

In Fig. 9c the u-velocity obtained for $\mathrm{Re} = 1000$ using (3.4) shows excellent agreement with [25]. The u-velocity profiles obtained from using the 40×40 stretched grids are presented for $\mathrm{Re} = 1000 \sim 10{,}000$ in Fig. 9c–f. A kink in the velocity profile is observed near the upper wall (i.e., $y = 1$) for very high Re (e.g., 5000 and 10,000). This would probably be unstable in the presence of small disturbances.

Each calculation has been done starting with an initial velocity field (i.e., $\mathbf{u}$ at $t = 0$) which is zero everywhere. Run conditions, convergence, CPU time, and others are listed in Table I, in which u_{max} and y_{max} denote respectively the maximum velocity of u and the corresponding y value near the bottom wall. Due to grid clustering near the wall, the representative velocity, q, is different from the value which is optimum for a uniform grid and the δ values appearing in Table I may not be optimum.

4. Conclusion and Recommendations

The present time marching finite-difference method using artificial compressibility has been applied to incompressible fluid flow through a channel and in a highly recirculating region. With a staggered grid and velocity–pressure couplings, the present central-difference scheme is stable and accurate in calculations of fluid flow through channels and in cavity for a wide range of Reynolds numbers without adding artificial damping terms. The present method is also stable for large cell Reynods numbers. For example, the cell Reynolds number appearing in the calculation of the driven cavity flow at $\mathrm{Re} = 10000$ is as high as about 100. No spatial oscillations in the flow variables are observed for high Re flow calculations.

It is recommended that a value for the artificial compressibility, δ, be chosen as in (2.16) by proper selection of q through the understanding of the flow of current interest together with a consideration of grid arrangement. For optimum values of δ and time step, however, further investigation including the viscous effects is needed. As for the Courant number, selecting too large a value should be avoided, since the Δt^2 term in (2.8) affects our scheme.

APPENDIX

The $(Ru)_{ij}$, $(Rv)_{ij}$, and $(Rp)_{ij}$ in (2.9) and (2.10) are written in the finite-difference form for each cell as

$$\frac{(Ru)_{ij}}{\Delta t}=\frac{1}{\mathrm{Re}}\left(\frac{u_{i+1j}+u_{i-1j}-2u_{ij}}{\Delta x^2}+\frac{u_{ij+1}+u_{ij-1}-2u_{ij}}{\Delta y^2}\right)-\frac{p_{i+1j}-p_{ij}}{\Delta x}$$
$$-\frac{(u_u^+)^2-(u_u^-)^2}{\Delta x}-\frac{v_u^+\cdot UUN-v_u^-\cdot UUS}{\Delta y}$$

$$\frac{(Rv)_{ij}}{\Delta t}=\frac{1}{\mathrm{Re}}\left(\frac{v_{i+1j}+v_{i-1j}-2v_{ij}}{\Delta x^2}+\frac{v_{ij+1}+v_{ij-1}-2v_{ij}}{\Delta y^2}\right)-\frac{p_{ij+1}-p_{ij}}{\Delta y}$$
$$-\frac{u_v^+\cdot VVE-u_v^-\cdot VVW}{\Delta x}-\frac{(v_v^+)^2-(v_v^-)^2}{\Delta y}$$

$$\frac{\delta}{\Delta t}(Rp)_{ij}=-\frac{u_{ij}-u_{i-1j}}{\Delta x}-\frac{v_{ij}-v_{ij-1}}{\Delta y}$$

where $UUN=(u_{ij}+u_{ij+1})/2$, $UUS=(u_{ij}+u_{ij-1})/2$, $VVE=(v_{ij}+v_{i+1j})/2$, and $VVW=(v_{ij}+v_{i-1j})/2$. At the cell whose boundary lies on the wall,

$$\frac{\partial^2 u}{\partial y^2}=\frac{4(u_{i2}/3-u_{i1})}{\Delta y^2}\quad\text{for}\quad j=1,\qquad\frac{4(u_{iJ-1}/3-u_{iJ})}{\Delta y^2}\quad\text{for}\quad j=J.$$

For the y-sweep, (2.10) can be rewritten as

$$A\,\Delta v^*_{ij-1}+B\,\Delta v^*_{ij}+C\,\Delta v^*_{ij+1}+t_y(\Delta p^*_{ij+1}-\Delta p^*_{ij})=(Rv)_{ij}\tag{A-1}$$

$$\frac{t_y}{\delta}(\Delta v^*_{ij}-\Delta v^*_{ij-1})+\Delta p^*_{ij}=(Rp)_{ij}\tag{A-2}$$

where $A=-(t_y/2)\,v_v^- - t'_y$, $B=1+(t_y/2)(v_v^+-v_v^-)+2t'_y$, and $C=(t_y/2)\,v_v^+-t'_y$. Subtracting (A-2) for $j=j+1$ from (A-2) for $j=j$ gives

$$\Delta p^*_{ij+1}-\Delta p^*_{ij}=(Rp)_{ij+1}-(Rp)_{ij}-\frac{t_y}{\delta}(\Delta v^*_{ij+1}+\Delta v^*_{ij-1}-2\,\Delta v^*_{ij}).$$

Then, (A-1) becomes

$$\left(A-\frac{t_y^2}{\delta}\right)\Delta v^*_{ij-1}+\left(B+\frac{2t_y^2}{\delta}\right)\Delta v^*_{ij}+\left(C-\frac{t_y^2}{\delta}\right)\Delta v^*_{ij+1}$$
$$=(Rv)_{ij}-t_y((Rp)_{ij+1}-(Rp)_{ij}).\tag{A-1'}$$

Equation (A-1′) can be solved for $j=1,\ldots,J-1$ ($\Delta v^*_{iJ}=0$ since v is given at the wall, i.e., $j=J$) using a tridiagonal matrix solver, then the Δp^*_{ij} in (A-2) is obtained subsequently.

For the x-sweep, (2.12) is rewritten as

$$D\Delta u_{i-1j}^{n+1} + E\,\Delta u_{ij}^{n+1} + F\,\Delta u_{i+1j}^{n+1} + t_x(\Delta p_{i+1j}^{n+1} - \Delta p_{ij}^{n+1}) = \Delta u_{ij}^{*} \tag{A-3}$$

$$\frac{t_x}{\delta}(\Delta u_{ij}^{n+1} - \Delta u_{i-1j}^{n+1}) + \Delta p_{ij}^{n+1} = \Delta p_{ij}^{*} \tag{A-4}$$

where D, E, and F are the first entries of the first, second, and third square matrices in (2.12). At $i=I$, $\Delta p_{i+1j}^{n+1} - \Delta p_{ij}^{n+1}$ in (A-3) becomes $-\Delta p_{ij}^{n+1}$ because the p, which is p_{I+1j} there, is given at the right-side boundary of the u-cell. Strictly speaking, p is not given fixed but varies with time about a fixed value, which is zero in the present study. The value of p_{I+1j} is evaluated at the nth time step using (3.1). As solution approaches steady-state p_{I+1j} becomes independent of time. For $i=I$, all of the convective terms are extrapolated to be $u_u^+ = u_{Ij} + (u_{Ij} - u_{I-1j})/2$, $v_u^+ = VVE = v_{Ij} + (v_{Ij} - v_{I-1j})/2$, and $v_u^- = v_{Ij-1} + (v_{Ij-1} - v_{I-1j-1})/2$. The diffusion terms are approximated as

$$\frac{\partial^2 u}{\partial x^2} = \frac{u_{I-2j} + u_{Ij} - 2u_{I-1j}}{\Delta x^2}, \qquad \frac{\partial^2 v}{\partial x^2} = \frac{v_{I-2j} + v_{Ij} - 2v_{I-1j}}{\Delta x^2}$$

As was the case with (A-1′), the above equation (A-3) can be written as

$$\left(D - \frac{t_x^2}{\delta}\right)\Delta u_{i-1j}^{n+1} + \left(E + \frac{2t_x^2}{\delta}\right)\Delta u_{ij}^{n+1} + \left(F - \frac{t_x^2}{\delta}\right)\Delta u_{i+1j}^{n+1} = \Delta u_{ij}^{*} - t_x(\Delta p_{i+1j}^{*} - \Delta p_{ij}^{*}). \tag{A-3′}$$

To observe the structure of the system (A-1′) and (A-3′), it is assumed that $v_v^+ = v_v^- = v$, $u_u^+ = u_u^- = u$, and that they are positive. If the cell Reynolds numbers, Re $v\,\Delta y$ and Re $u\,\Delta x$, are less than 2, (A-1′) and (A-3′) are diagonal dominant. For Re $v\,\Delta y$ and Re $u\,\Delta x$ much greater than 2 we can write (A-1′) and (A-3′) as

$$\left(-\frac{t_y}{2}v - \frac{t_y^2}{\delta}\right)\Delta v_{ij-1}^{*} + \left(1 + \frac{2t_y^2}{\delta}\right)\Delta v_{ij}^{*} + \left(\frac{t_y}{2}v - \frac{t_y^2}{\delta}\right)\Delta v_{ij+1}^{*} = \text{RHS of (A-1′)} \tag{A-5}$$

$$\left(-\frac{t_x}{2}u - \frac{t_x^2}{\delta}\right)\Delta u_{i-1j}^{n+1} + \left(1 + \frac{2t_x^2}{\delta}\right)\Delta u_{ij}^{n+1} + \left(\frac{t_x}{2}u - \frac{t_x^2}{\delta}\right)\Delta u_{i+1j}^{n+1} = \text{RHS of (A-3′)}. \tag{A-6}$$

For $(t_y/2)\,v < t_y^2/\delta$ and $(t_x/2)\,u < t_x^2/\delta$, (A-5) and (A-6) are diagonal dominant. In the case where $(t_y/2)\,v$ and $(t_x/2)\,u$ are larger than t_y^2/δ and t_x^2/δ, respectively, we have the following for the diagonal dominance:

$$u^2,\ v^2 < \frac{8}{\delta}.$$

Recalling that δ is chosen according to (2.16) we can conclude that the system (A-1′) and (A-3′) are always diagonal dominant in the practical calculation. However, the system (2.9) and (2.11) have some limitations on the time step to guarantee the diagonal dominance for the cell Reynolds numbers larger than 2 as

$$\frac{v\,\Delta t}{\Delta y} < \frac{1}{1-2(\mathrm{Re}\,v\,\Delta y)^{-1}}, \qquad \frac{u\,\Delta t}{\Delta x} < \frac{1}{1-2(\mathrm{Re}\,u\,\Delta x)^{-1}}$$

The above arguments about the diagonal dominance are confined only to the partial step, which is either an intermediate step or a correction step denoted by

correction step (A-3′) and (2.11). This may allow a large cell Reynolds number without deteriorating the present central difference numerical scheme. To confirm this in an affirmative way a rigorous stability analysis of the velocity–pressure coupled system is needed, which is not carried out in this paper.

Acknowledgments

The author is grateful to Dr. Peter M. Sockol and Professor Eli Turkel for providing valuable discussions, and is also indebted to Dr. Sin-Chung Chang and the referees for many criticisms and suggestions.

References

1. F. H. Harlow and J. E. Welch, *Phys. Fluids* **8** (1965), 2182.
2. G. P. Williams, *J. Fluid Mech.* **37** (1969), 727.
3. A. J. Chorin, *Math. Comput.* **22** (1968), 745.
4. C. W. Hirt and J. L. Cook, *J. Comput. Phys.* **10** (1972), 324.
5. C. S. Peskin, *J. Comput. Phys.* **10** (1972), 252.
6. N.-S. Liu, *INSERM-Euromech. 92* **71** (1977), 53.
7. A. J. Chorin, *J. Comput. Phys.* **2** (1967), 12.
8. R. Temam, *Arch. Rational Mech. Anal.* **32** (1969), 135 and **33** (1969), 377.
9. W. H. Plows, *Phys. Fluids* **12** (1968), 1593.
10. W. J. Grabowski and S. A. Berger, *J. Fluid Mech.* **75** (1976), 525.
11. W. Y. Soh and S. A. Berger, *J. Fluid Mech.* **84** (1984), 109.
12. J. L. C. Chang and D. Kwak, AIAA Paper 84-0252 (1984).
13. D. Choi and C. L. Merkle, *AIAA J.* **23** (1985), 1518.
14. E. Turkel, ICASE Report 86 14, 1986 (unpublished).
15. R. Peyret and T. D. Taylor, "Computational Methods for Fluid Flow," p. 144. Springer-Verlag, New York, 1983.
16. J. Douglas and J. E. Gunn, *Numer. Math.* **6** (1964), 428.
17. R. M. Beam and R. F. Warming, *J. Comput. Phys.* **22** (1976), 87.
18. W. R. Briley and H. McDonald, *J. Comput. Phys.* **34** (1980), 54.
19. J.-A. Essers, "Time-Dependent Methods for Mixed and Hybrid Steady Flows," von Karman Institute for Fluid Mechanics, Lecture Series 1978-4 (unpublished).

20. J. GILLIS AND A BRANDT, Air Force European Office of Aerospace Res. Sci. Rep. 63 (AD 614 915), 1964 (unpublished).
21. M. VAN DYKE, *J. Fluid Mech.* **44** (1970), 813.
22. J. R. BODOIA AND J. F. OSTERLE, *Appl. Sci. Res.* **10** (1961), 265.
23. Y. L. WANG AND P. A. LONGWELL, *AIChE. J.* **10** (1964), 323.
24. C. I. CHRISTOV, Orthogonal coordinate meshes with manageable Jacobian, *in* "Numerical Grid Generation" (J. F. Thompson, Ed.) p. 885, North-Holland, New York, 1982.
25. U. GHIA, K. N. GHIA, AND C. T. SHIN, *J. Comput. Phys.* **48** (1982), 387.